Science Bulletin 67 (2022) 2176–2185

Contents lists available at ScienceDirect

Science Bulletin

journal homepage: www.elsevier.com/locate/scib

Article

Titanium doped kagome superconductor $CsV_{3-x}Ti_xSb_5$ and two distinct phases

Haitao Yang [a,b,c,1], Zihao Huang [a,b,1], Yuhang Zhang [a,b,1], Zhen Zhao [a,b,1], Jinan Shi [b], Hailan Luo [a,b], Lin Zhao [a,b], Guojian Qian [a,b], Hengxin Tan [d], Bin Hu [a,b], Ke Zhu [a,b], Zouyouwei Lu [a,b], Hua Zhang [a,b], Jianping Sun [a,b], Jinguang Cheng [a,b], Chengmin Shen [a,b], Xiao Lin [b], Binghai Yan [d], Xingjiang Zhou [a,b], Ziqiang Wang [e], Stephen J. Pennycook [b,a], Hui Chen [a,b,c,*], Xiaoli Dong [a,b,*], Wu Zhou [b,c,*], Hong-Jun Gao [a,b,c,*]

[a] Beijing National Center for Condensed Matter Physics and Institute of Physics, Chinese Academy of Sciences, Beijing 100190, China
[b] School of Physical Sciences, University of Chinese Academy of Sciences, Beijing 100190, China
[c] CAS Center for Excellence in Topological Quantum Computation, University of Chinese Academy of Sciences, Beijing 100190, China
[d] Department of Condensed Matter Physics, Weizmann Institute of Science, Rehovot 7610001, Israel
[e] Department of Physics, Boston College, Chestnut Hill, MA 02467, USA

ARTICLE INFO

Article history:
Received 4 October 2022
Received in revised form 14 October 2022
Accepted 17 October 2022
Available online 19 October 2022

Keywords:
Kagome superconductor
Chemical doping
Charge density waves
Nematicity
Competing orders

ABSTRACT

The vanadium-based kagome superconductor CsV_3Sb_5 has attracted tremendous attention due to its unexcepted anomalous Hall effect (AHE), charge density waves (CDWs), nematicity, and a pseudogap pair density wave (PDW) coexisting with unconventional strong-coupling superconductivity. The origins of CDWs, unconventional superconductivity, and their correlation with different electronic states in this kagome system are of great significance, but so far, are still under debate. Chemical doping in the kagome layer provides one of the most direct ways to reveal the intrinsic physics, but remains unexplored. Here, we report, for the first time, the synthesis of Ti-substituted CsV_3Sb_5 single crystals and its rich phase diagram mapping the evolution of intertwining electronic states. The Ti atoms directly substitute for V in the kagome layers. $CsV_{3-x}Ti_xSb_5$ shows two distinct superconductivity phases upon substitution. The Ti slightly-substituted phase displays an unconventional V-shaped superconductivity gap, coexisting with weakening CDW, PDW, AHE, and nematicity. The Ti highly-substituted phase has a U-shaped superconductivity gap concomitant with a short-range rotation symmetry breaking CDW, while long-range CDW, twofold symmetry of in-plane resistivity, AHE, and PDW are absent. Furthermore, we also demonstrate the chemical substitution of V atoms with other elements such as Cr and Nb, showing a different modulation on the superconductivity phases and CDWs. These findings open up a way to synthesise a new family of doped CsV_3Sb_5 materials, and further represent a new platform for tuning the different correlated electronic states and superconducting pairing in kagome superconductors.

1. Introduction

The newly discovered kagome metals AV_3Sb_5 (A = K, Rb, Cs) have attracted tremendous research interest as a novel platform to study the interplay between nontrivial band topology, superconductivity, and multiple density waves [1–7]. The AV_3Sb_5 carries no magnetic order at low temperatures but exhibits an unconventional anomalous Hall effect (AHE) that is usually observed in ferromagnetic materials [8–10]. Most recently, unidirectional charge order [11,12], electronic nematicity [13] and roton pair density wave (PDW) [6] have been observed in the strong-coupling kagome superconductor CsV_3Sb_5. Time-reversal symmetry breaking (TRSB) was proposed to originate from the unconventional charge density waves (CDWs) [2,14], but this is still under debate [15–22]. The nature of the CDWs and superconducting states remains elusive. Theoretically, CsV_3Sb_5 has a Z_2 nontrivial topological band structure with topological surface states, indicating an unconventional superconductor [1,23], while some theoretical works propose the conventional s-wave superconductivity in CsV_3Sb_5. Experimentally, transport evidence for gap nodes [24] and gapless core states in magnetic-field induced vortices [3] have been reported, while tunneling diode oscillator [25] and nuclear quadrupole resonance [26] experiments showed the nodeless

[1] These authors contributed equally to this work.
* Corresponding authors.
E-mail addresses: hchenn04@iphy.ac.cn (H. Chen), dong@iphy.ac.cn (X. Dong), wuzhou@ucas.ac.cn (W. Zhou), hjgao@iphy.ac.cn (H.-J. Gao).

https://doi.org/10.1016/j.scib.2022.10.015
2095-9273/

superconductivity nature of CsV_3Sb_5. Therefore, full understanding of the pairing of the superconducting state and its correlation with the kagome geometry, TRSB, and rotational symmetry breaking orders remains an important issue to be urgently resolved.

Chemical doping and external pressure both provide effective ways to study the nature of the superconducting state and its correlation with the other orders. For example, double superconducting domes with enhanced superconductivity transition temperature have recently been observed in CsV_3Sb_5 upon applied pressure [5,27]. However, it is difficult to combine the high-pressure approaches with the local electronic states and band structures, which makes it hard to explore the interplay of CDWs, superconductivity, AHE, and nematicity. On the other hand, chemical doping via suitable partial element substitution can introduce carrier doping effect [28,29], impurity effect [11], and chemical pressure [30], not only for the induction of superconductivity but also serving as a "probe" for the exploration of the superconductivity mechanism. Specifically, cation substitution is one of the most effective ways for electron/hole doping in superconductors. For example, chemical substitutions in CuO_2 plane destroy the superconductivity in the cuprate superconductors revealing the importance of short-range antiferromagnetic correlation of Cu^{2+} ions [31], while some elements with the outermost electron configuration of d^7 and d^8 can induce superconductivity by doping in the superconducting-active Fe_2As_2 or FeSe layer in Fe-based superconductors, indicating the relevance of superconductivity to the itinerant *d*-electron and orbital fluctuation [32]. In kagome superconductor $LaRu_3Si_2$ with distorted kagome Ru layers, superconductivity is suppressed due to a strong influence of impurity effect via the substitution of Ru by transition metal ions including Fe, Co, Ni and Cr [33], and the subsequent muon spin relaxation (μSR) experiment and calculation suggest superconductivity is attributed to the kagome lattice related factors [34]. In a recent study, selective oxidation of exfoliated CsV_3Sb_5 thin flakes is reported to induce hole-doping to CsV_3Sb_5 and a superconducting dome was obtained as a function of doping content [35]. As the unusual properties are believed to come from the proximity of the V 3*d* orbitals close to the van Hove singularity (VHS), chemical substitution of the transition metal V in the kagome layer should be an effective way to directly tune the VHS and unveil the origin of intrinsic electronic structures of AV_3Sb_5, but remains so far unexplored.

In this work, we report the synthesis of titanium-substituted $CsV_{3-x}Ti_xSb_5$ single crystals for the first time. We demonstrate that the nonmagnetic Ti atoms mainly substitute the V sites in the kagome layer through high-resolution scanning transmission electron microscopy (STEM) chemical imaging combined with density functional calculations. Low-temperature scanning tunneling microscopy/spectroscopy (STM/S) reveals that both long-range $2a_0 \times 2a_0$ and $4a_0$ CDW and $4a_0/3 \times 4a_0/3$ PDW gradually disappear as the titanium content (labelled as *x*) increases. The magnetic susceptibility and transport measurements indicate that, as *x* increases, the onset temperatures of long-range CDW, nematicity, and AHE gradually decrease and are absent at around $x = 0.09$, unequivocally demonstrating that the AHE and nematicity are strongly correlated to the long-range CDW. In addition, as *x* increases, T_c firstly drops to a minimum value and then increases to 3.7 K, showing a double-dome shape in the phase diagram. Importantly, the Ti slightly substituted region shows an unconventional superconductivity phase with a V-shaped gap, coexisting with long-range CDWs, nematicity, and AHE, whereas the Ti highly-substituted phase displays a conventional superconductivity phase with a U-shaped gap coexisting with a short-range $4a_0$ CDW. These results demonstrate that the $CsV_{3-x}Ti_xSb_5$ exhibits two distinct superconductivity phases with different correlated electronic states. The angle-resolved photoemission spectra (ARPES) measurements demonstrate that the Fermi level relatively shifts to higher energy and the VHS at M point shifts across the Fermi level as *x* increases, which may result in the suppression of CDW, AHE, and nematicity.

2. Materials and methods

2.1. Single crystal growth of the Ti-substituted CsV_3Sb_5 samples

Single crystals of X-substituted (X = Ti, Cr and Nb) CsV_3Sb_5 were grown from Cs liquid (purity 99.98%), V powder (purity 99.9%), Ti, Cr or Nb shot (purity > 99.9%) and Sb shot (purity 99.999%) via a modified self-flux method [36]. The mixture was put into an alumina crucible and sealed in a quartz ampoule under Argon atmosphere. The mixture was heated to 1000 °C and soaked for 24 h, and subsequently cooled at 2 °C/h. Finally, the single crystals were separated from the flux and the residual flux on the surface was carefully removed by Scotch tape. Except for sealing and heat treatment procedures, all other preparation procedures were carried out in an argon-filled glove box in order to avoid the introduction of any air and water. The obtained crystals have a typical hexagonal morphology with a maximum size of over $10 \times 7 \times 0.3$ mm^3 (Fig. 1b) and are stable in air.

2.2. Sample characterization

X-ray diffraction (XRD) patterns were collected using a Rigaku SmartLab SE X-ray diffractometer with Cu K_α radiation (λ = 0.15406 nm) at room temperature. Scanning electron microscopy (SEM) and X-ray energy-dispersive spectroscopy (EDS) were performed using a HITACHI S5000 with an energy dispersive analysis system Bruker XFlash 6|60. Magnetic susceptibility and magnetization oscillation were determined by a SQUID magnetometer (Quantum Design MPMS XL-1 and MPMS-3). The superconductivity transition of each sample was monitored down to 2 K under an external magnetic field of 1 Oe. Both in-plane electrical resistivity and Hall resistivity data were collected on a Quantum Design Physical Properties Measurement System (PPMS). Samples with different doping contents were dissolved by aqua regia for inductively coupled plasma (ICP) measurements.

2.3. Scanning transmission electron microscopy and electron energy-loss spectroscopy

Two cross-sectional samples along the [1 0 0] and [2 1 0] projections were prepared from the $CsV_{3-x}Ti_xSb_5$ ($x = 0.15$) single crystal using a focused ion beam (FIB) system. Atomic-scale STEM imaging and electron energy-loss spectroscopy (EELS) analyses were carried out on an aberration-corrected Nion U-HERMES100 dedicated STEM, operated at 60 kV. The probe forming angle was set to 32 mrad, and the probe current was set to 120 pA. The high-angle annular dark-field (HAADF) and annular bright field (ABF) images were collected from the 75–250 and 15–30 mrad angular ranges, respectively. The EELS collection angle was set to 75 mrad. In order to reduce random noise in the EELS data, the STEM-EELS chemical mappings shown in the main text and the Supplementary materials (online) have been denoised using principal component analysis (PCA). Quantification of the Ti:V ratio was calculated based on the integrated EELS signals of the two elements and the corresponding inelastic scattering cross-sections under the same experimental conditions. Note that this analysis is only semi-quantitative due to errors in calculating the inelastic scattering cross-sections for the different element edges.

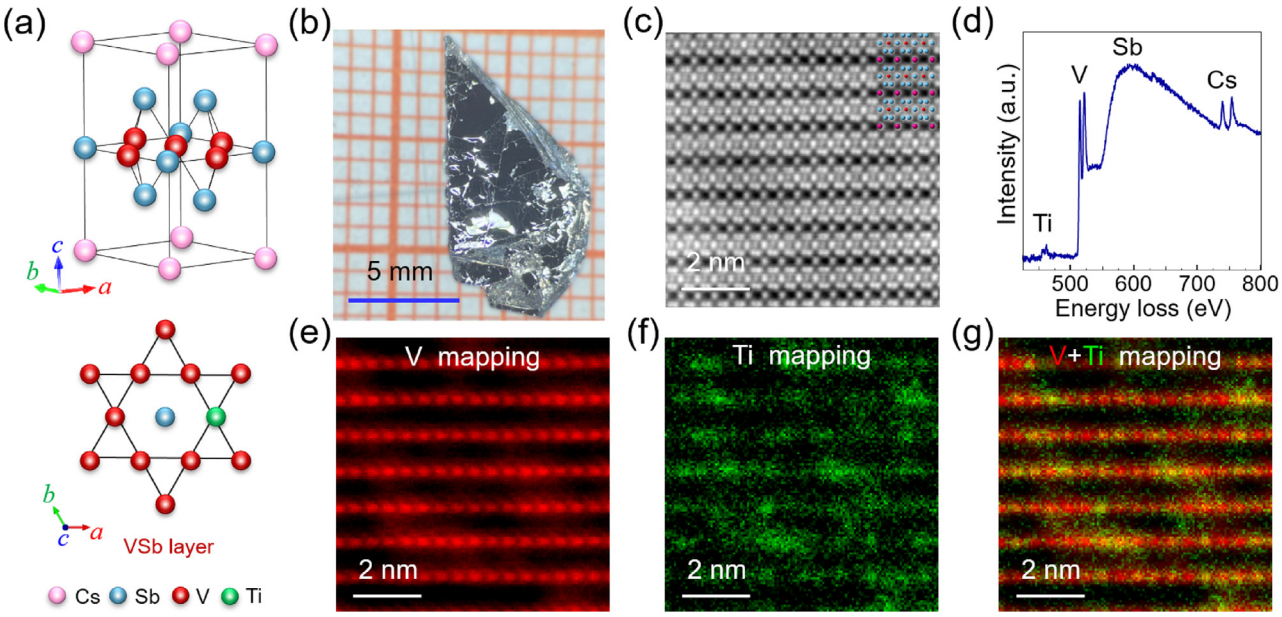

Fig. 1. Determination of the Ti substitution positions in $CsV_{3-x}Ti_xSb_5$ single crystals. (a) Schematic of atomic structure of Ti-substituted $CsV_{3-x}Ti_xSb_5$ crystal with Cs atoms in light purple, Sb atoms in light blue, V atoms in red and Ti atoms in green. The Ti atoms replace the V atoms in the kagome lattice. (b) A photo of a single crystal of the as-prepared $CsV_{3-x}Ti_xSb_5$ (x = 0.15) crystal. (c) STEM-HAADF Z-contrast image of $CsV_{3-x}Ti_xSb_5$ crystal viewed along the [100] projection, with the atomic structural models overlaid. The Cs, V, Sb atoms are shown in purple, red, and light blue, respectively. (d) Background-subtracted EELS spectrum showing clear Ti, V, Sb, and Cs signals. Quantification of the Ti and V signals shows an atomic ratio of Ti:V ~5.3:94.7. (e, f) Atomic-resolution chemical mapping acquired via STEM-EELS spectrum imaging, with the simultaneously acquired V mapping shown in red (e) and Ti mapping shown in green (f). (g) Overlay of the V (red) and Ti (green) signals. Ti is mostly doped into the V sites.

2.4. Scanning tunneling microscopy/spectroscopy

The samples used in the experiments were cleaved at a low temperature (about 13 K) and immediately transferred to an STM chamber. Experiments were performed in an ultrahigh vacuum (1×10^{-10} mbar) ultra-low temperature STM system equipped with 11 T magnetic field. The electronic temperature in the low-temperature STS is 650 mK, calibrated using a standard superconductor, Nb crystal [37]. All the scanning parameters (setpoint voltage and current) of the STM topographic images are listed in the figure captions. Unless otherwise noted, the dI/dV spectra were acquired by a standard lock-in amplifier at a modulation frequency of 973.1 Hz. The tungsten tips were fabricated via electrochemical etching and calibrated on a clean Au(111) surface prepared by repeated cycles of sputtering with argon ions and annealing at 500 °C. To eliminate the STM tip-drift effect from the topography and dI/dV map, we apply the well-known Lawler-Fujita algorithm [38], after subtracting a 2nd or 3rd degree polynomial background, and obtain a set of displacement fields and drift-corrected topography. The so-obtained displacement fields are then applied to the simultaneously measured dI/dV maps in the same field of view as the topography.

2.5. Density-functional theory (DFT) calculations

Calculations are performed within the DFT as implemented in VASP package [39]. The generalized-gradient-approximation as parametrized by Perdew-Burke-Ernzerhof [40] for the exchange–correlation interaction between electrons is employed in all calculations. Zero damping DFT-D3 vdW correction [41] is also employed in all calculations while the spin-orbital coupling is not included. The supercell method is used to calculate the formation energy. The supercells with Ti substitutions are fully relaxed until the remaining forces on the atoms are less than 0.005 eV/Å. The k-meshes of $6 \times 6 \times 3$ and $3 \times 3 \times 4$ are used to sample the Brillouin zones of the $2 \times 2 \times 2$ and $3 \times 3 \times 1$ supercells of CsV_3Sb_5, respectively. A cutoff energy of 300 eV for the plane-wave basis set is used.

2.6. High resolution ARPES measurements

High-resolution angle-resolved photoemission measurements were carried out on our lab system using ultraviolet laser as the light source that can provide a photon energy of $h\nu$ = 6.994 eV with a bandwidth of 0.26 meV. The energy resolution was set at ~2.5 meV for the measurements. The angular resolution is ~0.3°. The Fermi level is referenced by measuring on a clean polycrystalline gold that is electrically connected to the sample. The sample was cleaved *in situ* and measured in vacuum with a base pressure better than 5×10^{-11} Torr.

3. Results and discussions

3.1. Determination of the Ti substitution positions in $CsV_{3-x}Ti_xSb_5$ crystals

We have successfully grown Ti-substituted $CsV_{3-x}Ti_xSb_5$ crystals with different substitution ratios ranging from x = 0.00 to 0.27. The as-grown $CsV_{3-x}Ti_xSb_5$ single crystals (Methods) exhibit a stacking sequence of Cs-Sb2-VSb1-Sb2-Cs layers with hexagonal symmetry (space group P 6/mmm). In the VSb1 layer, the kagome sub-lattice of vanadium is interwoven with a simple hexagonal sub-lattice formed by the Sb1 atoms. As Ti is the neighboring non-magnetic element to V, the ionic radii of Ti^{4+} (60.5 pm) and V^{5+} (54.0 pm) ion are similar, which results in a high possibility of Ti substitution at the V sites in the kagome lattice (Fig. 1a). A typical $CsV_{3-x}Ti_xSb_5$ crystal with a lateral size of over 1 cm and regular shape is shown in Fig. 1b. Smaller and thinner $CsV_{3-x}Ti_xSb_5$ single crystals showing regular hexagonal morphology (Fig. S1a online), were also obtained. The Ti substitution content of a typical $CsV_{3-x}Ti_xSb_5$ single crystal determined by the EDS is x = 0.15 as shown in Fig. S1b (online), corresponding to 5% substitution of V.

The representative XRD pattern and the rocking curve confirm the high-quality of the $CsV_{3-x}Ti_xSb_5$ single crystal with a preferred [0 0 1] orientation (Fig. S1c and d online). The lattice parameters *a*, *b*, and *c* are measured to be 5.521, 5,521 and 9.336 Å, respectively, by single crystal diffraction, which are slightly smaller than those of pristine CsV_3Sb_5 (5.548, 5.548 and 9.349 Å, respectively). The lattice change is only about 0.4% and 0.1% in *a* and *c* axis, respectively, indicating a negligible chemical pressure.

To confirm the successful substitution of Ti into the CsV_3Sb_5 lattice, we carried out atomic-scale structural and chemical analysis on cross-sectional samples using aberration corrected STEM. Fig. 1c shows a typical STEM HAADF Z-contrast image [42] of the $CsV_{3-x}Ti_xSb_5$ (x = 0.15) sample along the [1 0 0] projection, with the structural models overlaid. The image clearly reveals the perfect crystalline structure of the $CsV_{3-x}Ti_xSb_5$ sample without noticeable structural defects, suggesting that Ti substitution does not degrade the crystal quality. The distinct sequential layers of Cs-Sb2-VSb1-Sb2-Cs are further confirmed by the elemental mapping shown in Fig. S2 (online). Chemical analysis via EELS unambiguously confirms the presence of Ti atoms (Fig. 1d), with the overall Ti substitution of V measured to be ~5%, which is consistent with the EDS and ICP measurements. The spatial distribution of the Ti atoms is revealed by the atomic-resolution chemical mapping shown in Fig. 1e–g. By comparing the simultaneously acquired V map (Fig. 1e) and Ti map (Fig. 1f), it is clear that most of the Ti atoms are located in the VSb1 layer, coinciding with the V atomic columns. Imaging and chemical analysis of the cross-sectional sample along the [2 1 0] projection (Fig. S3 online) reveal similar information. These results, thus, suggest that the majority of Ti atoms is substituting the V sites in the CsV_3Sb_5 lattice.

In order to understand the substitution mechanism, we estimated the formation energy of Ti substitution in CsV_3Sb_5 by DFT calculations. We examined different Ti substitution contents and varied distances between neighboring Ti atoms. We found that the formation energy is in the range of −2.2 – −2.3 eV per Ti atom, which is insensitive to the Ti–Ti distance in the lattice (see more details in Fig. S4 online). The negative formation energies indicate that Ti atoms in CsV_3Sb_5 are energetically favored. The insensitivity of the formation energy to Ti-Ti distance suggests the uniform distribution of Ti atoms inside CsV_3Sb_5, which is consistent with the observation by STEM.

3.2. Evolution of correlated electronic states in $CsV_{3-x}Ti_xSb_5$ crystals

We investigated the responses of CDW, AHE, and superconducting transitions to the substitution of Ti in $CsV_{3-x}Ti_xSb_5$ single crystals via the combination of magnetization, specific heat capacity, and electrical transport measurements. The superconductivity in $CsV_{3-x}Ti_xSb_5$ crystals with x between 0.00 and 0.27 was examined by diamagnetism and resistivity measurements. Bulk superconductivity with onset temperature T_c^M is evidenced by the superconducting diamagnetism, as shown in Fig. 2a. It clearly shows that T_c^M decreases to about 2.5 K at x = 0.04 and then increases to 3.7 K at x = 0.27. Importantly, the bulk superconductivity is confirmed by the 100% shield effect in $CsV_{3-x}Ti_xSb_5$ (x = 0.04) based on the superconductivity diamagnetism monitored down to 0.4 K (Fig. S5a online). The onset superconducting transition temperature (T_c^R) derived from the temperature-dependent normalized resistivity of the pure CsV_3Sb_5 is above 4.0 K, about 0.5 K higher than that of the $CsV_{3-x}Ti_xSb_5$ (x = 0.15) crystal (Fig. S5b online). However, after applying different magnetic fields ranging from 0.02 to 1 T, the T_c^R of the pure CsV_3Sb_5 shifts to lower temperatures with a broadening transition behavior, resembling the features of broad superconductivity transitions observed in copper-oxide and iron-based high-temperature superconductors [43–45], In contrast, the T_c^R of the $CsV_{3-x}Ti_xSb_5$ (x = 0.15) crystal decreases rapidly with applied fields showing a conventional superconductivity behavior similar to that of MgB_2 [46].

To further investigate the Ti substitution effect on the normal state properties of this kagome superconductor system, systematic electrical transport measurements were conducted. Firstly, the CDW transition temperature (T_{CDW}) shows an obvious decrease from ~94 to ~60 K with increasing substitution contents, as evidenced by kinks in the temperature-dependent resistivity curves of $CsV_{3-x}Ti_xSb_5$ (x = 0.00, 0.03, and 0.04) crystals (Fig. 2b and Fig. S5c online). The kink fades out in $CsV_{3-x}Ti_xSb_5$ (x = 0.09, 0.15, and 0.27) crystals, indicating the absence of long-range CDWs. The temperature-dependent specific heat-capacity measurements (Fig. S5d online) also provide strong evidences for the undetectability of long-range CDWs in $CsV_{3-x}Ti_xSb_5$ (x = 0.09, 0.15, and 0.27) crystals.

We performed Hall measurements on $CsV_{3-x}Ti_xSb_5$ crystals with different substitution contents at various temperatures (Fig. S6a–e online). ρ_{xy} of the $CsV_{3-x}Ti_xSb_5$ crystal (x = 0.03, 0.04) exhibits a linear behavior at high temperature and an antisymmetric sideways "S" line shape at low fields below T_{CDW}, which is similar to those of pure CsV_3Sb_5 due to the AHE. In contrast, ρ_{xy} of $CsV_{3-x}Ti_xSb_5$ crystals (x = 0.09, 0.15) show a linear behavior over the entire range of external fields under different temperatures. Unlike a significant enhancement of hole mobility of pure CsV_3Sb_5 at low temperature as a multiband system [9], Hall coefficients R_H of $CsV_{3-x}Ti_xSb_5$ crystals are negative within a wide temperature range from 150 K down to 2 K, indicating that electron-type carriers are dominant (Fig. S6f online). A gradual increase of the absolute value R_H can be observed upon substitution contents. ρ_{xy}^{AHE} of $CsV_{3-x}Ti_xSb_5$ crystals (x = 0.03 and 0.04) persists up to about 60 K (Fig. S6g, h online) and ρ_{xy}^{AHE} of $CsV_{3-x}Ti_xSb_5$ crystals (x = 0.09) demonstrates no AHE. The anomalous Hall conductivity (AHC) σ_{xy}^{AHE} of $CsV_{3-x}Ti_xSb_5$ crystals (x = 0.03 and 0.04) clearly shows the sudden appearance of the AHE below T_{CDW} and the values of σ_{xy}^{AHE} decreases with the Ti substitution increasing (Fig. 2c), which is possibly due to the suppression of the long-range CDWs.

We also measured the in-plane angular-dependent magnetoresistance (AMR) of $CsV_{3-x}Ti_xSb_5$ (x = 0.03, 0.04, 0.09, and 0.15) crystals under a field of 5 T at different temperatures above T_c. The ratios of AMR defined as $\Delta R/R_{min} = [R(\theta, T) - R_{min}(T)]/R_{min}(T) \times 100\%$ are summarized in Fig. S7 (online) by polar-coordinate plots. AMR of $CsV_{3-x}Ti_xSb_5$ (x = 0.00, 0.03, 0.04) crystals appear below T_{CDW} and the ratios of AMR decrease with the increasing Ti substitution content. The $CsV_{3-x}Ti_xSb_5$ (x = 0.09 and 0.15) crystals show no AMR signals in their normal states (Fig. S7f online). The ratios of AMR at 5 K indicates clearly the absence of the twofold rotational symmetry with high Ti substitution content of x = 0.09 (Fig. 2d), namely the suppression of nematicity by Ti substitution [47].

To understand the evolution of CDW, AHE, and AMR in $CsV_{3-x}Ti_xSb_5$ crystals, the band structures crossing Brillioun zone center Γ along Γ-K direction for different Ti substitution contents of x = 0.00, 0.04, 0.15, and 0.27 have been performed at 20 K by high-resolution VUV laser ARPES (Fig. S8 online). An electron like band around Γ point (α band) is present for all the Ti-substituted samples. At x = 0.00, some extra bands around Γ just below the Fermi level (E_F) and around the binding energies between 0.4 and 0.8 eV can be observed. These bands are from the band folding of those around M points due to the 2 × 2 reconstruction in the CDW state [48]. They are absent for the $CsV_{3-x}Ti_xSb_5$ samples, which is consistent with our results that the long-range CDW state is suppressed by the Ti substitution (Fig. S8a online). The energy distribution curves (EDCs) at Γ point (Fig. S8b online) show the energy positions shift up monotonously by about 5, 10 and 100 meV for the $CsV_{3-x}Ti_xSb_5$ samples (x = 0.04, 0.15 and 0.27)

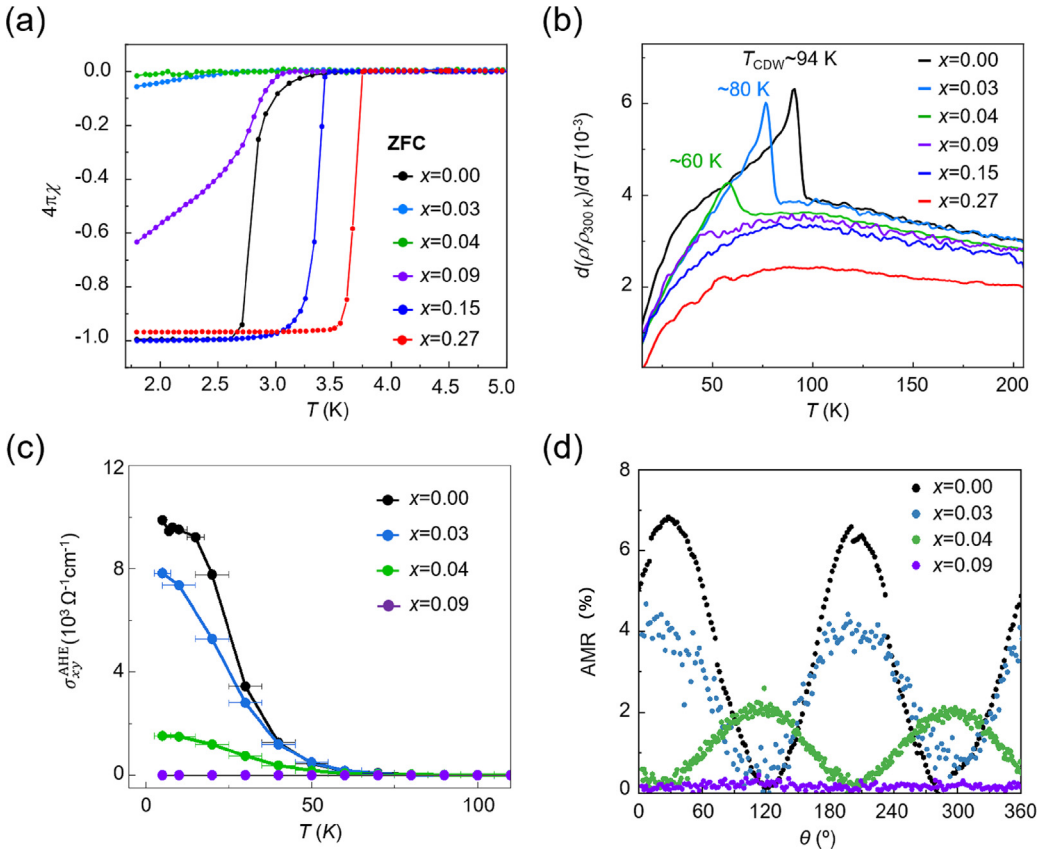

Fig. 2. Ti substitution effects on superconductivity, CDW, AHE, and AMR in $CsV_{3-x}Ti_xSb_5$ crystals. (a) The temperature-dependent magnetic susceptibilities corrected for demagnetization factor under zero-field cooling (ZFC) with applied field of 1 Oe along the *c* axis. (b) The derivative electrical resistivity dρ/dT curve of $CsV_{3-x}Ti_xSb_5$ crystals with x from 0.00 to 0.27. The CDW is suppressed upon increasing x and undetectable when x exceeds 0.09. (c) The anomalous Hall conductivity of $CsV_{3-x}Ti_xSb_5$ (x = 0.00, 0.03, 0.04, and 0.09) crystals as a function of temperature obtained by subtracting the local linear ordinary Hall conductivity background. (d) The in-plane AMR equated to $\Delta R/R_{min}$ as a function of θ at T = 5 K. Here θ is the angle between the directions of the external field (H) of 5 T and the current (I), with θ = 0° corresponding to H // I.

as compared to that of the pure sample. The shift of 100 meV for $CsV_{3-x}Ti_xSb_5$ samples (x = 0.27) clearly indicates that the hole doping pushes the Fermi level downwards. The DFT calculations also demonstrate that with increasing Ti substitution the Fermi energy moves down with slight dispersion changes (Fig. S8c, d online). The above ARPES and DFT results indicate that the substitution of Ti is an efficient way to tune the Fermi level of the CsV_3Sb_5 system by hole doping.

Comparing the band structures around M point and Γ point between the CsV_3Sb_5 and $CsV_{3-x}Ti_xSb_5$ (x = 0.27) samples (Fig. S9 online), the bands just below E_F around M (marked by pink and purple lines in Fig. S9c online) in the pure CsV_3Sb_5, representing the VHS2 bands marked in Fig. S8d (online), are absent (pink) or crossing the E_F (purple) around M point in the $CsV_{3-x}Ti_xSb_5$ (x = 0.27) sample (Fig. S9d online). The ARPES results clearly indicate that the VHS2 of electronic structures at *M* point shifts across over the Fermi level after Ti substitution in the kagome lattice. Therefore, we conclude that the suppression of electron scattering around *M* points, and the corresponding suppression of CDW, originates from the crossing of VHS2 point above E_F at M point. The suppression of CDW results in the suppression of other correlated electronic states including AHE, AMR, and nematicity.

3.3. Local electronic structures of $CsV_{3-x}Ti_xSb_5$ crystals

We then studied the evolution of CDW on the surface of the $CsV_{3-x}Ti_xSb_5$ samples with various Ti substitution contents at the atomic scale by low temperature STM/S (Fig. 3). In the STM measurements, almost all the surface regions show large-scale Cs surface topography. Large-scale Sb surface topography was rarely observed. Because of the reconstruction of Cs terminated surface (Fig. S10 online) and its possible surface doping effect [49,50], we choose Sb surface to study the evolution of CDWs. We applied the STM manipulation method to sweep the top Cs atoms away to expose large-scale Sb surfaces [6]. In both STM topography ($T(\boldsymbol{r}, V)$) and dI/dV maps (dI/d$V(\boldsymbol{r}, V)$) of the large-scale Sb surface, we found that, as compared to the pure CsV_3Sb_5 sample [6], many small spots with darker intensity appear and randomly distribute in the STM images of the Sb surface. Atomically resolved STM images demonstrate that the Sb lattice remains continuous across the dark spots (inset in Fig. 3a), indicating that the dark spots originate from electron scattering in the underlying VSb1 layer. We then analyzed the height histogram of the STM images of the Sb surface and found that the area density of the dark spots shows a positive correlation with the Ti substitution contents (Fig. S11 online), which further qualitatively demonstrates that the dark spots in the STM images originate from Ti atoms in the underlying VSb1 kagome layer.

In addition to the emergence of dark spots, there are significant changes of the CDW in both STM images and dI/dV mapping of the $CsV_{3-x}Ti_xSb_5$ samples as compared with the pure CsV_3Sb_5 sample. We find that the bidirectional $2a_0 \times 2a_0$ (green circles in Fig. 3c) and unidirectional $4a_0$ CDWs (red squares in Fig. 3c) at all energies (details in Fig. S12 online) are preserved for the slightly-substituted $CsV_{3-x}Ti_xSb_5$ samples (x = 0.03 in Fig. 3a–c and x = 0.04 in Fig. 3d–f). However, both $2a_0 \times 2a_0$ and $4a_0$ CDWs almost disappear in the Fourier transform of the topography and dI/dV mapping of the x = 0.15 sample (Fig. 3g–i).

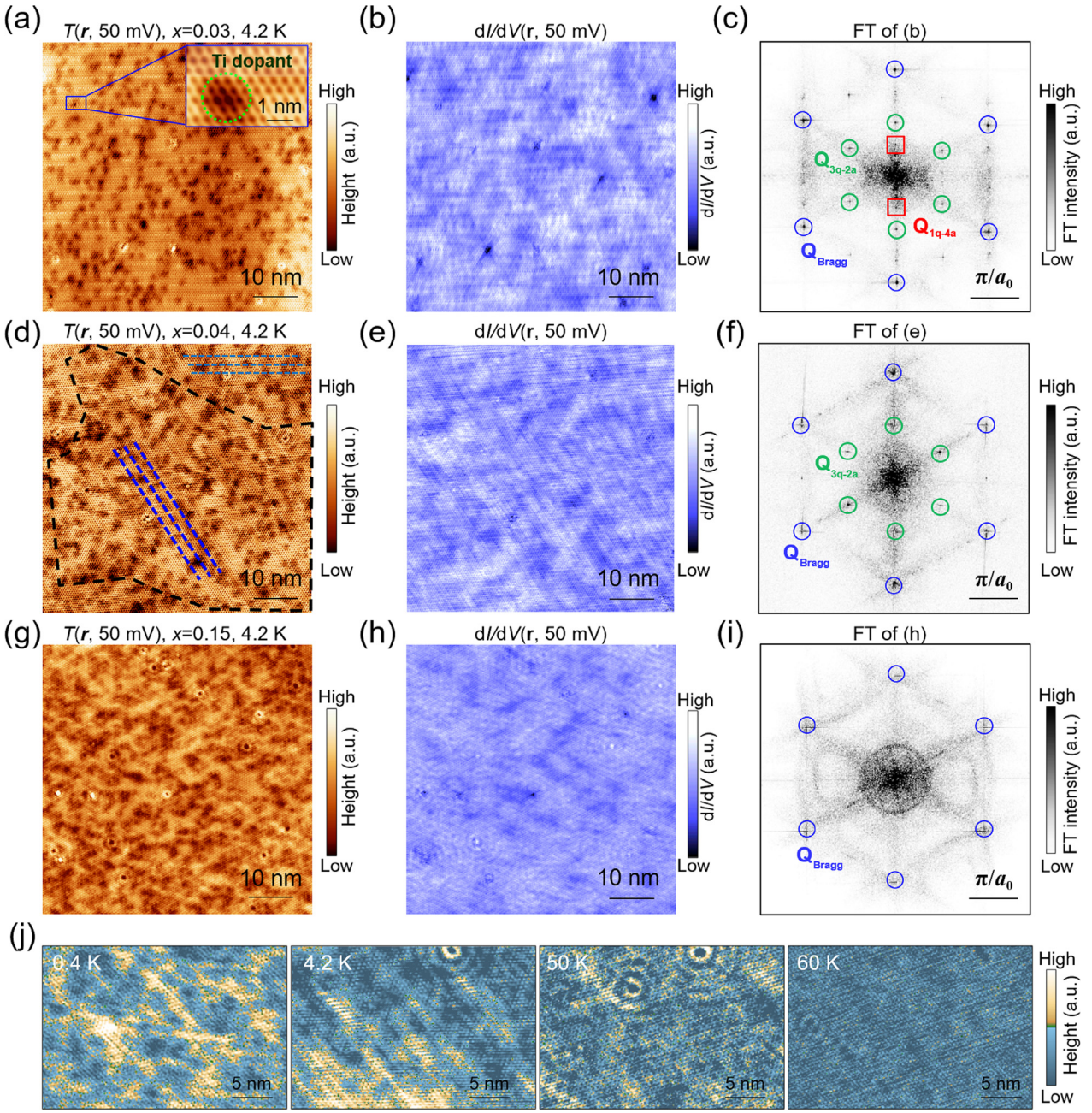

Fig. 3. Local electronic structures of $CsV_{3-x}Ti_xSb_5$ crystals. (a–c) STM topography (a), d*I*/d*V*(*r*, 50 mV) (b) and the corresponding drift-corrected Fourier transform (FT) (c) at the large-scale Sb surface of $CsV_{3-x}Ti_xSb_5$ (x = 0.03) obtained at 4.2 K, showing the 3Q-2*a* and 1Q-4*a* CDWs. Many dark spots, correlated to the Ti atoms, appear in the STM image of (a). The inset in (a): Zoom-in STM image showing the continuous lattice around the dark spots. (d–f) STM topography (d), d*I*/d*V*(*r*, −5 mV) (e) and the corresponding drift-corrected FT (f) at the large-scale Sb surface of $CsV_{3-x}Ti_xSb_5$ (x = 0.04), showing the presence of short-range 1Q-4*a* CDW multiple domains. Two 4*a* CDW domains can be clearly observed (highlighted by blue and light blue dotted lines). (g–i) STM topography (g), d*I*/d*V*(*r*, 50 mV) (h) and the corresponding drift-corrected FT (i) at the large-sized Sb surface of $CsV_{3-x}Ti_xSb_5$ (x = 0.15), showing the absence of 3Q-2*a*, and long-range 1Q-4*a* CDW states in the FT. The weak and elongated stripes around M points in (i) result from QPI pattern instead of long-range 3Q-2*a* CDWs. Setting parameter: tunneling current setpoint I_t = 1.0 nA. (j) STM images of the Sb surface of $CsV_{3-x}Ti_xSb_5$ (x = 0.15) at 0.4, 4.2, 50, and 60 K, respectively, showing that the short-range charge orders disappear at a critical temperature of ~60 K. v_s = −50 mV, I_t = 1.0 nA.

The simultaneous suppression and disappearance of long-range $2a_0 \times 2a_0$ and $4a_0$ charge orders strongly indicate that these two CDWs are intertwined with each other. It should be noticed that, the bidirectional $4/3a_0$ PDW peaks [6] (labeled by pink circles in Fig. S12a, b online) in the Fourier transform of d*I*/d*V* maps at low energy (less than 5 meV) are suppressed in the x = 0.03 and 0.04 samples but invisible in the x = 0.15 sample (Fig. S12c online), suggesting that the PDW is intertwined with $2a_0 \times 2a_0$ and $4a_0$ CDWs.

Although the peaks correspond to the long-range $2a_0 \times 2a_0$ and $4a_0$ CDWs in the FT are too weak to be observed, short-range striped orders can be clearly seen in the topography of the $CsV_{3-x}Ti_xSb_5$ (x = 0.15) sample (Fig. 3j). Furthermore, the temperature-dependent STM images of the Sb surface of $CsV_{3-x}Ti_xSb_5$ (x = 0.15) show that the short-range stripe orders disappear at a critical temperature of ~55 K (Fig. 3j), similar to the critical temperature in the pure CsV_3Sb_5 [51].

3.4. Microscopic evolution of superconductivity and phase diagram of $CsV_{3-x}Ti_xSb_5$ crystals

To reveal the microscopic evolution of superconductivity in $CsV_{3-x}Ti_xSb_5$ crystals, we lowered the electron temperature to

650 mK (Fig. S13 online) and collected a series of d*I*/d*V* spectra at both Sb and Cs surfaces (Fig. S10 online). Because the superconducting gap size is found to be homogenous despite some variations in the coherence peak height and gap depth in different regions of sample surface (Fig. S14 online), we use the spatially-averaged d*I*/d*V* spectra over tens of regions for comparison. We find that the x = 0.03 sample shows a V-shaped paring gap (blue curve in Fig. 4a) corresponding to a nodal superconducting phase, whereas the x = 0.15 and 0.27 samples show a conventional Bardeen–Cooper–Schrieffer (BCS) gap (details please see Figs. S15 and S16 online) corresponding to a nodeless superconducting phase (green and dark green curve in Fig. 4a). The V-shaped pairing gap in the x = 0.03 sample is slightly smaller than that of the pure sample (black curve), and the zero-bias conductance is much higher than that in the pure sample, indicating the decrease of T_c. For the x = 0.15 and 0.27 samples, the superconductivity paring is totally different from the pure and slightly substituted samples, demonstrating the transition into a new superconductivity phase.

Fig. 4b presents the phase diagram of $CsV_{3-x}Ti_xSb_5$ single crystals, where the onset temperatures of long-range three-dimensional CDW (T_{CDW}) and superconductivity (T_c), together with the amplitude of AHE and AMR (top panel), are summarized as a function of substitution content x. Both T_{CDW} and T_c are suppressed with increasing Ti substitution and T_{CDW} becomes absent below x = 0.09, accompanied by the strongly correlated evolution of the AHE and AMR amplitude (Fig. 4b upper panel), clearly demonstrating that they are strongly correlated with each other. In addition, the $CsV_{3-x}Ti_xSb_5$ system shows two superconducting phases. In the Ti slightly-substituted phase, the superconducting state shows a V-shape pairing gap coexisting with long-range charge orders, AHE and AMR. The T_c decreases from ~3.5 K of the pure CsV_3Sb_5 sample to ~2.0 K of the x = 0.04 sample. In the Ti highly-substituted phase, the T_c increases from ~2.0 K (x = 0.04) to ~3.7 K (x = 0.27). This superconducting phase exhibits the U-shaped gap pairing and a sharp superconductivity transition at the expense of T_c under magnetic field (Fig. S5b online, solid lines). Although the long-range charge orders are undetectable in the second phase, there are still short-range stripe orders, which indicates the coexistence of correlated electronic states and U-shaped superconductivity featuring parallels to iron-based superconductors. To our knowledge, $CsV_{3-x}Ti_xSb_5$ is the first kagome superconductor reported so far that two distinct superconductivity phases emerge upon chemical substitution at ambient pressure, strongly correlating with CDW, AHE, and AMR. Such a transition from V-shaped to U-shaped superconducting phase is rare in the study of superconductivity, and is analogous to the twisted trilayer graphene [52].

It is worth noting that the V kagome layer substitution is not limited to Ti. We further explored the substitution of V with elements in the same periodic or the same group elements of V. Using the same synthesis method, we have successfully prepared $CsV_{3-x}Cr_xSb_5$ (x = 0.06 and 0.15) and $CsV_{3-x}Nb_xSb_5$ (x = 0.03 and 0.06) crystals through substitution of V ions in the kagome layer with Cr (Cr^{5+}≃49.0 pm) and Nb (Nb^{4+}≃68.0 pm). For the Cr-substituted samples, the superconductivity is suppressed

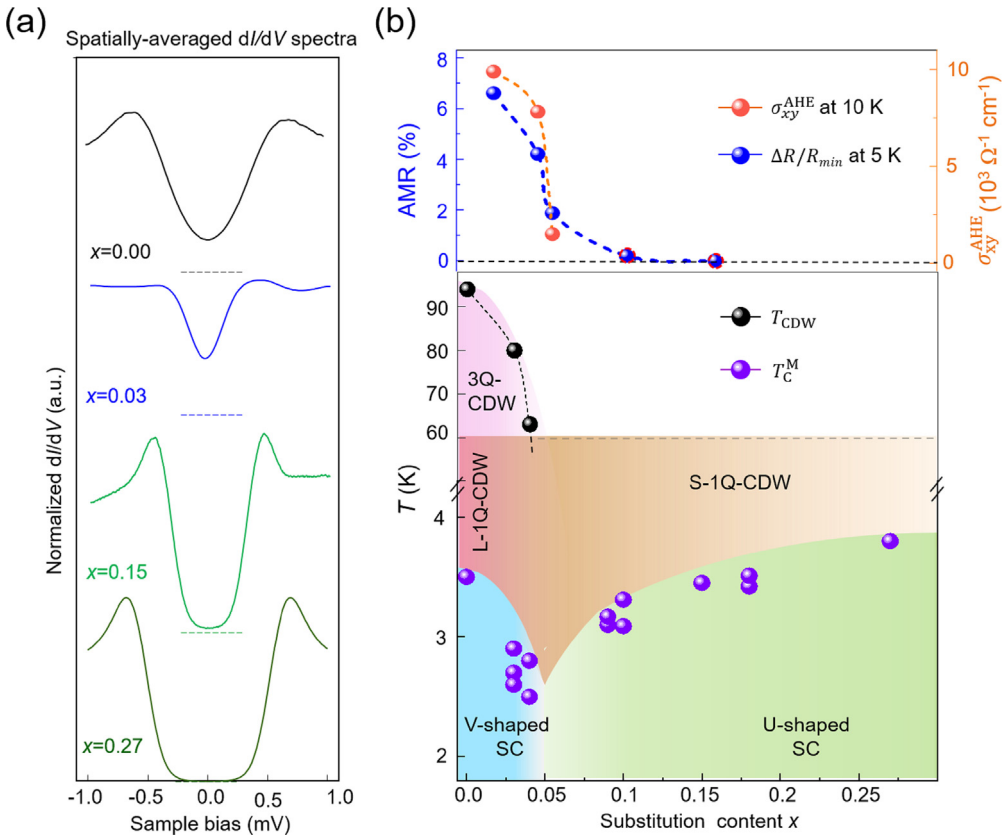

Fig. 4. Phase diagram of $CsV_{3-x}Ti_xSb_5$ crystals. (a) Spatially-averaged d*I*/d*V* spectra obtained on the Sb surfaces of the CsV_3Sb_5 (black curve) and $CsV_{3-x}Ti_xSb_5$ samples (x = 0.03, 0.04, 0.15 and 0.27, corresponding to blue, green, and dark green curves, respectively), showing a transition from V-shape to U-shape symmetry through Ti substitution. The horizontal dash lines highlight the positions of zero density of states for each curve. (b) Phase diagram of the $CsV_{3-x}Ti_xSb_5$ crystals. In the V-Shaped superconductivity regime, T_{CDW} is significantly reduced with increasing x. The amplitude of the anomalous Hall conductivity σ_{xy}^{AHE} and AMR (%), is dramatically decreased, that is, long-range CDW, AHE and nematicity were simultaneously suppressed. In contrast, in the U-shaped superconductivity regime where AHE, long-range CDW, and nematicity are undetectable, the superconductivity coexisting with short-range CDWs tends to gradually recover: T_c^M rises to ~3.5 K at x = 0.15, and showing a slight increase to 3.7 K at x = 0.27.

dramatically as Cr substitution content increases and becomes undetectable at x = 0.15, and the CDW features become significantly weaker (Fig. S17 online). In contrast, for the Nb-substituted samples, the superconductivity is enhanced (T_c is 4.2 K for x = 0.06, which is higher than 3.5 K of CsV_3Sb_5) and CDW signals fade gradually as Nb substitution content increases (Fig. S18 online). Therefore, the present work opens up a way to synthesise a new family of doped kagome materials by various substitution elements, and represents a new platform for tuning the correlated electronic states including charge orders, loop current, nematicity and superconducting pairing.

4. Summary

We report, for the first time, the synthesis of Ti-doped vanadium-based kagome superconductor $CsV_{3-x}Ti_xSb_5$. STEM demonstrates that the V atoms in the kagome layers are directly substituted by the Ti atoms. $CsV_{3-x}Ti_xSb_5$ exhibits two distinct superconductivity phases upon substitution. The Ti slightly-substituted phase displays an unconventional V-shaped superconductivity gap, coexisting with weakening CDW, PDW, AHE, and nematicity. The Ti highly-substituted phase has a U-shaped superconductivity gap concomitant with a short-range rotation symmetry breaking CDW, while long-range CDW, twofold symmetry of in-plane resistivity, AHE, and PDW are absent. The high-quality single crystals with controlled Ti substitution contents in kagome planes provide a new platform allowing for systematic study of the evolution of superconductivity with multiple intertwining orders (CDW, PDW, AHE, and nematicity) in both macroscopic and microscopic views, which is not possible with high-pressure approaches and/or polycrystalline samples. The double-dome superconductivity only indicates the change of T_c, whereas the microscopic evolution of superconductivity pairing upon chemical doping and pressure is more important for understanding the kagome-lattice based physics. We discover a unique phase exhibiting U-shaped superconductivity gap concomitant with short-range rotation-symmetry breaking orders in the highly-substituted crystals, featuring parallels to iron-based superconductors. Such a transition from V-shaped to U-shaped transition superconducting phases concomitant with the evolution of the long-rang to short-rang CDW provides a rare platform in the study of superconductivity. The systematic and detailed mechanism of the competing orders in the Ti-doped CsV_3Sb_5 by both experiments and theory needs further studies in the future.

Note: after completion of this manuscript, we found that another chemical (Sn) doped CsV_3Sb_5 was synthesized and published independently [53].

Conflict of interest

The authors declare that they have no conflict of interest.

Acknowledgments

The work was supported by grants from the National Natural Science Foundation of China (61888102, 52022105, 51771224, 11888101, 12061131005, and 11834016), the National Key Research and Development Projects of China (2018YFA0305800 and 2019YFA0308500), the Chinese Academy of Sciences (XDB33030100, XDB28010200, and XDB30010000), the Key Research Program of Chinese Academy of Sciences (ZDBS-SSW-WHC001), the CAS Project for Young Scientists in Basic Research (YSBR-003) and the Beijing Outstanding Young Scientist Program (BJJWZYJH01201914430039). Z.W. is supported by the US DOE, Basic Energy Sciences Grant (DE-FG02-99ER45747). B.Y. acknowledges the financial support by the European Research Council (ERC Consolidator Grant, No. 815869) and the Israel Science Foundation (ISF No. 1251/19). We thank Zhong-Xian Zhao and Gang Su for helpful discussions.

Author contributions

Hong-Jun Gao supervised and coordinated the project. Hong-Jun Gao and Haitao Yang designed the research. Haitao Yang and Zhao Zhen prepared the samples. Yuhang Zhang, Zouyouwei Lu, Hua Zhang, Jianping Sun, Jinguang Cheng, Haitao Yang, and Xiaoli Dong performed the transport experiments. Hui Chen, Zihao Huang, Guojian Qian, and Bin Hu performed the STM experiments with the guidance of Hong-Jun Gao. Wu Zhou, Jinan Shi, and Stephen J. Pennycook performed the STEM experiments. Hailan Luo, Lin Zhao, and Xingjiang Zhou perform the ARPES experiments. Tengxin Tan and Binghai Yan performed the DFT calculations. All authors participated in the data analysis and manuscript writing.

Appendix A. Supplementary materials

Supplementary materials to this article can be found online at https://doi.org/10.1016/j.scib.2022.10.015.

References

[1] Ortiz BR, Teicher SML, Hu Y, et al. CsV_3Sb_5: a Z_2 topological kagome metal with a superconducting ground state. Phys Rev Lett 2020;125:247002.
[2] Jiang Y-X, Yin J-X, Denner MM, et al. Unconventional chiral charge order in kagome superconductor KV_3Sb_5. Nat Mater 2021;20:1353–7.
[3] Liang Z, Hou X, Zhang F, et al. Three-dimensional charge density wave and surface-dependent vortex-core states in a kagome superconductor CsV_3Sb_5. Phys Rev X 2021;11:031026.
[4] Yu FH, Ma DH, Zhuo WZ, et al. Unusual competition of superconductivity and charge-density-wave state in a compressed topological kagome metal. Nat Commun 2021;12:3645.
[5] Chen KY, Wang NN, Yin QW, et al. Double superconducting dome and triple enhancement of T_c in the kagome superconductor CsV_3Sb_5 under high pressure. Phys Rev Lett 2021;126:247001.
[6] Chen H, Yang H, Hu B, et al. Roton pair density wave in a strong-coupling kagome superconductor. Nature 2021;599:222–8.
[7] Broyles C, Graf D, Yang H, et al. Effect of the interlayer ordering on the Fermi surface of Kagome superconductor CsV_3Sb_5 revealed by quantum oscillations. Phys Rev Lett 2022;129:157001.
[8] Yang S-Y, Wang Y, Ortiz BR, et al. Giant, unconventional anomalous Hall effect in the metallic frustrated magnet candidate, KV_3Sb_5. Sci Adv 2020;6:eabb6003.
[9] Yu FH, Wu T, Wang ZY, et al. Concurrence of anomalous Hall effect and charge density wave in a superconducting topological kagome metal. Phys Rev B 2021;104:L041103.
[10] Kenney EM, Ortiz BR, Wang C, et al. Absence of local moments in the kagome metal KV_3Sb_5 as determined by muon spin spectroscopy. J Phys Condens Matter 2021;33:235801.
[11] Terashima K, Matsui H, Hashimoto D, et al. Impurity effects on electron–mode coupling in high-temperature superconductors. Nat Phys 2006;2:27–31.
[12] Hu B, Ye Y, Huang Z, et al. Robustness of the unidirectional stripe order in the kagome superconductor CsV_3Sb_5. Chin Phys B 2022;31:058102.
[13] Nie L, Sun K, Ma W, et al. Charge-density-wave-driven electronic nematicity in a kagome superconductor. Nature 2022;604:59–64.
[14] Mielke C, Das D, Yin JX, et al. Time-reversal symmetry-breaking charge order in a kagome superconductor. Nature 2022;602:245–50.
[15] Miao H, Li HX, Lee HN, et al. Geometry of the charge density wave in kagome metal AV_3Sb_5. Phys Rev B 2021;104:195132.
[16] Christensen MH, Birol T, Andersen BM, et al. Theory of the charge-density wave in AV_3Sb_5 kagome metals. Phys Rev B 2021;104:214513.
[17] Gu Y, Zhang Y, Feng X, et al. Gapless excitations inside the fully gapped kagome superconductors AV_3Sb_5. Phys Rev B 2021;105:L100502.
[18] Tan H, Liu Y, Wang Z, et al. Charge density waves and electronic properties of superconducting kagome metals. Phys Rev Lett 2021;127:046401.
[19] Feng XL, Zhang Y, Jiang K, et al. Low-energy effective theory and symmetry classification of flux phases on the kagome lattice. Phys Rev B 2021;104:16513.
[20] Denner MM, Thomale R, Neupert T. Analysis of charge order in the kagome metal AV_3Sb_5 (A=K, Rb, Cs). Phys Rev Lett 2021;127:217601.
[21] Wu XX, Schwemmer T, Muller T, et al. Nature of unconventional pairing in the kagome superconductors AV_3Sb_5 (A = K, Rb, Cs). Phys Rev Lett 2021;127:177001.
[22] Chen H, Hu B, Ye Y, et al. Superconductivity and unconventional density waves in vanadium-based kagome materials AV_3Sb_5. Chin Phys B 2022;31:097405.

[23] Ortiz BR, Sarte PM, Kenney EM, et al. Superconductivity in the Z_2 kagome metal KV_3Sb_5. Phys Rev Mater 2021;5:034801.
[24] Zhao CC, Wang LS, Xia W, et al. Nodal superconductivity and superconducting dome in the topological Kagome metal CsV_3Sb_5. Arxiv:2102.08356, 2021.
[25] Duan W, Nie Z, Luo S, et al. Nodeless superconductivity in the kagome metal CsV_3Sb_5. Sci China Phys Mech Astron 2021;64:107462.
[26] Mu C, Yin Q, Tu Z, et al. S-wave superconductivity in kagome metal CsV_3Sb_5 revealed by $^{121/123}$Sb NQR and ^{51}V NMR measurements. Chin Phys Lett 2021;38:077402.
[27] Yu F, Zhu X, Wen X, et al. Pressure-induced dimensional crossover in a kagome superconductor. Phys Rev Lett 2022;128:077001.
[28] Ideta S, Yoshida T, Nishi I, et al. Dependence of carrier doping on the impurity potential in transition-metal-substituted FeAs-based superconductors. Phys Rev Lett 2013;110:107007.
[29] Luetkens H, Klauss HH, Kraken M, et al. The electronic phase diagram of the $LaO_{1-x}F_xFeAs$ superconductor. Nat Mater 2009;8:305–9.
[30] Sun R, Jin S, Deng J, et al. Chemical pressure boost record-high superconductivity in van der Waals materials $FeSe_{1-x}S_x$. Adv Funct Mater 2021;31:2102917.
[31] Pan SH, Hudson EW, Lang KM, et al. Imaging the effects of individual zinc impurity atoms on superconductivity in $Bi_2Sr_2CaCu_2O_{8+\delta}$. Nature 2000;403:746–50.
[32] Ren ZA, Zhao ZX. Research and prospects of iron-based superconductors. Adv Mater 2009;21:4584–92.
[33] Li BX, Li S, Wen HH. Chemical doping effect in the $LaRu_3Si_2$ superconductor with a kagome lattice. Phys Rev B 2016;94:09452.
[34] Mielke C, Qin Y, Yin JX, et al. Nodeless kagome superconductivity in $LaRu_3Si_2$. Phys Rev Mater 2021;5:034803.
[35] Song Y, Ying T, Chen X, et al. Competition of superconductivity and charge density wave in selective oxidized CsV_3Sb_5 thin flakes. Phys Rev Lett 2021;127:237001.
[36] Ortiz BR, Gomes LC, Morey JR, et al. New kagome prototype materials: discovery of KV_3Sb_5, RbV_3Sb_5, and CsV_3Sb_5. Phys Rev Mater 2019;3:094407.
[37] Wang D, Kong L, Fan P, et al. Evidence for Majorana bound states in an iron-based superconductor. Science 2018;362:333–5.
[38] Lawler MJ, Fujita K, Lee J, et al. Intra-unit-cell electronic nematicity of the high-T_c copper-oxide pseudogap states. Nature 2010;466:347–51.
[39] Kresse G, Furthmuller J. Efficiency of ab-initio total energy calculations for metals and semiconductors using a plane-wave basis set. Comp Mater Sci 1996;6:15–50.
[40] Perdew JP, Burke K, Ernzerhof M. Generalized gradient approximation made simple. Phys Rev Lett 1996;77:3865–8.
[41] Grimme S, Antony J, Ehrlich S, et al. A consistent and accurate *ab initio* parametrization of density functional dispersion correction (DFT-D) for the 94 elements H-Pu. J Chem Phys 2010;132:154104.
[42] Pennycook SJ, Boatner LA. Chemically sensitive structure-imaging with a scanning-transmission electron-microscope. Nature 1988;336:565–7.
[43] Dong X, Jin K, Yuan D, et al. $(Li_{0.84}Fe_{0.16})$ $OHFe_{0.98}Se$ superconductor: Ion-exchange synthesis of large single-crystal and highly two-dimensional electron properties. Phys Rev B 2015; 92: 064515.
[44] Safar H, Gammel PL, Huse DA, et al. Experimental evidence for a first-order vortex-lattice-melting transition in untwinned, single crystal $YBa_2Cu_3O_7$. Phys Rev Lett 1992;69:824–7.
[45] Blatter G, Feigel'man MV, Geshkenbein VB, et al. Vortices in high-temperature superconductors. Rev Mod Phys 1994;66:1125.
[46] Eltsev Y, Lee S, Nakao K, et al. Anisotropic superconducting properties of MgB_2 single crystals probed by in-plane electrical transport measurements. Phys Rev B 2002;65:140501.
[47] Xiang Y, Li Q, Li Y, et al. Twofold symmetry of c-axis resistivity in topological kagome superconductor CsV_3Sb_5 with in-plane rotating magnetic field. Nat Commun 2021;12:6727.
[48] Luo H, Gao Q, Liu H, et al. Electronic nature of charge density wave and electron-phonon coupling in kagome superconductor KV_3Sb_5. Nat Commun 2022;13:273.
[49] Nakayama K, Li Y, Kato T, et al. Carrier injection and manipulation of charge-density wave in kagome superconductor CsV_3Sb_5. Phys Rev X 2022;12:011001.
[50] Yu J, Xu Z, Xiao K, et al. Evolution of electronic structure in pristine and Rb-reconstructed surfaces of kagome metal RbV_3Sb_5. Nano Lett 2022;22:918–25.
[51] Zhao H, Li H, Ortiz BR, et al. Cascade of correlated electron states in the kagome superconductor CsV_3Sb_5. Nature 2021;599:216–21.
[52] Kim H, Choi Y, Lewandowski C, et al. Evidence for unconventional superconductivity in twisted trilayer graphene. Nature 2022;606:494–500.
[53] Oey YM, Ortiz BR, Kaboudvand F, et al. Fermi level tuning and double-dome superconductivity in the kagome metal $CsV_3Sb_{5-x}Sn_x$. Phys Rev Mater 2022;6:L041801.

Haitao Yang is a professor at Institute of Physics, Chinese Academy of Sciences (IOP-CAS). He obtained his Ph.D. degree from IOP-CAS in 2004. He was a postdoctor at Tohoku University, Japan from 2004 to 2008. His current research interest mainly focuses on superconductivity, spin polarization, and electron correlated states of crystals and low dimensional materials.

Zihao Huang obtained his B.S. degree from University of Chinese Academy of Sciences in 2018, and now is a Ph.D. student at IOP-CAS, supervised by Prof. Hong-Jun Gao. His research interest focuses on the emergent physics of quantum materials, by using low-temperature scanning tunneling microscopy/spectroscopy.

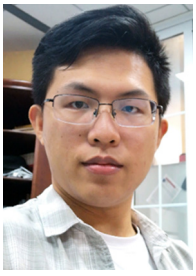

Yuhang Zhang obtained his B.S. degree from University of Chinese Academy of Sciences in 2019, and now is a Ph.D. candidate at IOP-CAS, supervised by Prof. Xiaoli Dong. His research interest includes novel superconducting properties revealed by delicate magnetic and electrical transport measurements, the underlying physics based on phenomenological theory analysis of superconducting critical parameters, and vortex physics of FeSe-based superconductors by magnetic force microscopy.

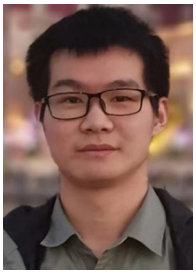

Zhen Zhao obtained his B.S. degree from Jilin University in 2019, and now is a Ph.D. candidate at IOP-CAS, supervised by Prof. Hong-Jun Gao. His research interest focuses on the discovery and synthesis of new superconducting materials combined with the study of novel physical properties.

Hui Chen is an associate professor at IOP-CAS. He got his Ph.D. degree from IOP-CAS. His current research interest mainly focuses on the atomic manipulation of low-dimensional quantum structures and novel proprieties of correlated and topological materials, using low-temperature scanning tunneling microcopy/spectroscopy.

Xiaoli Dong is a professor of Physics at National Lab for Superconductivity, IOP-CAS. Her research group at IOP-CAS focuses on the exploration of new superconductors and investigation of their underlying physics. Her current research interest includes exploring FeSe-based superconductors with high critical parameters by soft-chemical methods, and revealing the novel properties of unconventional superconductors by delicate magnetic and electrical transport measurements.

Wu Zhou is a Professor at School of Physical Sciences and leads the electron microscopy laboratory at the University of Chinese Academy of Sciences (UCAS) in Beijing, China. His research is mainly focused on the development of cutting-edge electron microscopy techniques with high spatial and energy resolution, and the application of electron microscopy to unveil the origin of functionalities in 2D materials, heterogenous catalysts and quantum materials.

Hong-Jun Gao received his Ph.D. degree in Physics from Peking University in 1994. He became a Professor at IOP-CAS in 1995. He is an Academician of the Chinese Academy of Sciences, an Academician of the Developing-Country Academy of Sciences (TWAS), and an Academician of the German National Academy of Sciences. His research interest focuses on the construction and physical properties of quantum nanostructures including two-dimensional atomic/molecular crystals, and scanning tunneling microscopy/spectroscopy.